



Dandelion-like cobalt oxide microsphere-supported RuCo bimetallic catalyst for highly efficient hydrogenolysis of 5-hydroxymethylfurfural

Zhi Gao*, Guoli Fan, Mengran Liu, Lan Yang, Feng Li*

State Key Laboratory of Chemical Resource Engineering, Beijing Advanced Innovation Center for Soft Matter Science and Engineering, Beijing University of Chemical Technology, Beijing, 100029, PR China

ARTICLE INFO

Keywords:

Bimetallic RuCo nanoparticles
Surface defects
Hydrogenolysis
5-Hydroxymethylfurfural
Biomass conversion

ABSTRACT

Currently, renewable biomass-derived energy sources and related transformation technologies are attracting numerous attentions due to the rapid consumption of fossil fuels and resulting increasing environmental pollution. Herein, a new dandelion-like cobalt oxide (CoO_x) microsphere-supported bimetallic RuCo catalyst was fabricated by a simple one-pot embedding method and employed for the 5-hydroxymethylfurfural (HMF) hydrogenolysis to produce liquid 2,5-dimethylfuran (DMF) biofuel. It was found that bimetallic RuCo nanoparticles (NPs) with the average size of about 2.5 nm could homogeneously disperse on flower-like CoO_x microspheres possessing abundant surface defects (i.e. oxygen vacancies and Co^{2+} species) simultaneously constructed. As-fabricated RuCo/ CoO_x catalyst exhibited excellent catalytic performance in above reaction, along with a quite high DMF yield of 96.5% at a high HMF/Ru molar ratio of 252.7, which was correlated with the unique synergy between bimetallic RuCo NPs and abundant surface defects at the metal-support interface, as well as the enhanced hydrogen spillover effect and the dandelion-like superstructure of the catalyst. Additionally, the strong interactions between RuCo species and the CoO_x matrix in the RuCo/ CoO_x significantly prevented RuCo NPs from migration, aggregation, and leaching during the reaction. The present findings offer a new approach for designing other highly efficient and stable bimetallic catalysts applied in a variety of heterogeneous catalytic systems.

1. Introduction

Energy and environment have always been two essential elements for the development and survival of human society. Currently, non-renewable fossil fuels (i.e. coal, oil and natural gas) are rapidly depleted, which causes the emission of large quantities of toxic and hazardous substances in use [1,2]. To develop renewable alternatives to meet the growing energy demand and eliminate the resulting increasing environmental pollution, the innovation of new production routes and related technologies for transportation fuels through upgrading renewable biomass resources is attracting more and more attention in scientific and industrial communities [3–10]. For instance, 5-hydroxymethylfurfural (HMF), as one of the most important platform chemicals in the field of biomass transformation, can be obtained from biomass-derived carbohydrates [11–13]. Further, HMF can be converted to a variety of important chemicals, such as 2,5-furandicarboxylic acid (FDCA), 2,5-diformylfuran (DFF), 2,5-dihydroxymethylfuran (BHMF), 2,5-dihydroxymethyltetrahydrofuran (DHMTFH) and highly promising fuel additive 2,5-dimethylfuran

(DMF) [14–19]. Among these chemicals, DMF especially possesses unique properties including high energy density, high octane number and low boiling point, which are superior to those of ethanol. In a word, DMF is a more appropriate and promising renewable liquid transportation fuel than dominant ethanol liquid fuel.

At present, significant efforts have been made to explore catalytic hydrogenolysis of HMF to produce DMF using noble metal catalysts [15,20–25]. For example, Román-Leshkov et. al reported the HMF hydrogenolysis over CuRu/C catalysts, along with a 71% DMF yield using molecular hydrogen at 220 °C for 10 h [15], despite the easy deactivation of the catalyst. A Ru-doped hydrotalcite catalyst could afford a DMF yield of 58% at 220 °C for 4 h [20]. When using formic acid as hydrogen source and Pd/C catalysts, a high DMF yield of 95% could be achieved [21]. Recently, Abu-Omar et. al reported an effective bimetallic catalyst combination containing a Lewis-acidic Zn(II) and Pd/C components for this reaction [24]. In addition, the HMF hydrogenolysis was also conducted over copper-containing porous metal oxide (Cu-PMO) in supercritical methanol [26]. However, above most catalytic systems require harsh reaction conditions, such as high catalyst

* Corresponding authors.

E-mail addresses: gaozhi910201@163.com (Z. Gao), lifeng@mail.buct.edu.cn (F. Li).

loading, high reaction temperatures and/or long reaction times, indicating that these catalysts are unfavorable for practical applications. Therefore, more efficient catalytic systems for HMF hydrogenolysis into DMF still need to be further explored.

As we know, surface geometric and electronic structures of catalysts have great influence on catalytic reactions [27]. In this regard, some reducible oxide supports (e.g. In_2O_3 [28], Co_3O_4 [29]) have been employed in hydrogenation reactions, thanks to the easy construction of surface oxygen vacancies (O_v). Recently, we also found that surface oxygen vacancies could be developed by the transformation of Mn^{3+} in supports to Mn^{2+} species [30]. Therefore, Mn^{2+} defects adjacent to oxygen vacancies could strongly interact with the oxygen atom in carbonyl group, thus resulting in the enhanced catalytic performance of Cu-based catalysts in the hydrogenation of dimethyl succinate. Therefore, to achieve the high efficiency of supported catalysts, finely controlling the microstructure of supports is of great importance.

Nowadays, bimetallic nanocatalysts are intensively investigated in a wide range of heterogeneous catalytic reactions [31,32], thanks to unique synergistic effects between two metals that can induce superior properties to their corresponding monometallic counterparts. In addition to the reduced cost of catalysts, the coordination of a base metal into precious metal can generate specific new active sites in bimetallic catalysts that originate from the unexpected electronic and geometrical effects between two metals. As for HMF hydrogenolysis to DMF, active hydrogen species need to selectively react with the formyl and hydroxyl groups without deep hydrogenation or ring-opening of furan. It was reported that bimetallic PtCo catalysts were effective for the reduction of C=O bond in α , β -unsaturated aldehydes, due to unique electronic and structural effects existing in PtCo nanoparticles (NPs) [33–35]. Moreover, in regards to supported bimetallic catalysts, the improvement in the dispersion and stability of bimetallic NPs remains a challenging task, despite successful synthesis of unsupported monometallic and bimetallic NPs [36–38].

Herein, we reported a facile one-pot embedding method (Scheme 1) for the synthesis of new bimetallic RuCo NPs embedded into dandelion-like CoO_x microspheres (RuCo/CoO_x). It was demonstrated that as-fabricated bimetallic RuCo catalyst with abundant surface $\text{Co}^{2+}-\text{O}_v-\text{Co}^{2+}$ defects could efficiently catalyze the HMF hydrogenolysis to produce DMF with a high DMF yield of 96.5% at a high HMF/Ru molar ratio of 252.7. Such high efficiency of the catalyst was correlated with the Ru-Co synergistic effect in RuCo NPs, favorable surface defects in proximal CoO_x sites, enhanced hydrogen spillover effect, as well as more active sites and reaction centers provided by the distinct dandelion-like nano/microstructure of CoO_x microspheres.

2. Experimental section

2.1. Synthesis of catalysts

RuCo/CoO_x sample with the theoretical Ru loading of 3 wt.% was prepared by our developed one-pot embedding method. Firstly, $\text{CoSO}_4 \cdot 6\text{H}_2\text{O}$ (7 mmol), $\text{CO}(\text{NH}_2)_2$ (10.5 mmol) and $\text{RuCl}_3 \cdot 3\text{H}_2\text{O}$ (0.15 mmol) were dissolved in 80 mL of distilled water to form a red mixed solution. Then, the solution was transferred into an autoclave (100 mL) with a Teflon liner, followed by hydrothermal treatment at 165 °C for 6 h. The resulting dark red precipitate was separated by centrifugation and washed with distilled water and alcohol for several times until the pH = 7.0. The product was dried in a vacuum oven at 70 °C for 12 h and then calcined at 500 °C for 6 h with a ramp of 2 °C min^{-1} . Finally, the as-calcined $\text{RuO}_2/\text{Co}_3\text{O}_4$ sample was reduced in 10% H_2/N_2 atmosphere at 300 °C for 2 h at a ramp rate of 5 °C min^{-1} to obtain the resulting reduced sample (denoted as RuCo/CoO_x). In addition, pristine flower-like Co_3O_4 or $\text{Ru/Al}_2\text{O}_3$ sample was prepared by the above same method as that for $\text{RuO}_2/\text{Co}_3\text{O}_4$ in the absence of $\text{RuCl}_3 \cdot 3\text{H}_2\text{O}$ or as that for RuCo/CoO_x using $\text{Al}_2(\text{SO}_4)_3$ instead of $\text{CoSO}_4 \cdot 6\text{H}_2\text{O}$, respectively. And, Co/CoO_x sample was prepared using the same procedure as that for RuCo/CoO_x without the addition of $\text{RuCl}_3 \cdot 3\text{H}_2\text{O}$.

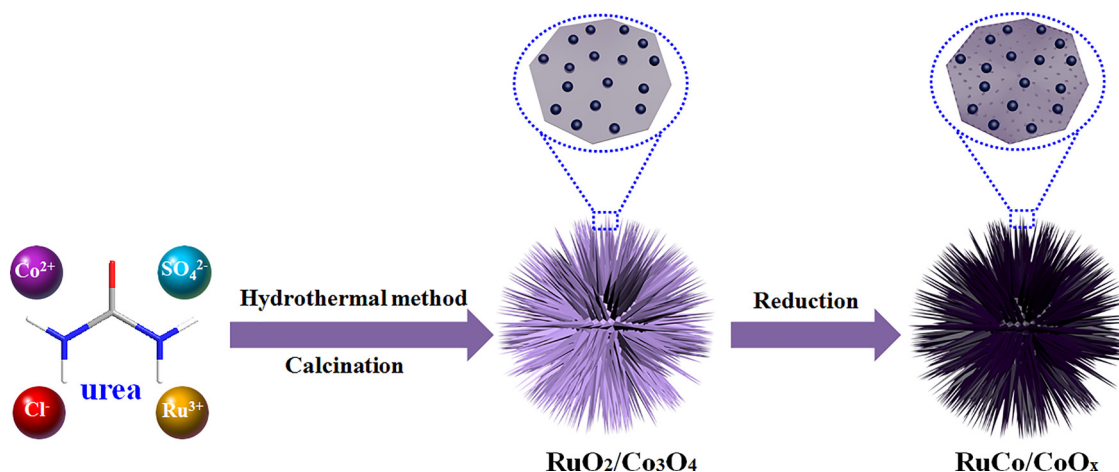
For comparison, $\text{Ru/Co}_3\text{O}_4$ -B and Ru/Co/CoO_x -B samples with a Ru loading of 3 wt. % were prepared using NaBH_4 reducing agent. Firstly, Co/CoO_x (0.5 g) or flower-like Co_3O_4 (0.5 g) and $\text{RuCl}_3 \cdot 3\text{H}_2\text{O}$ solution (0.15 mmol) were added into 100 mL of distilled water under ultrasonication for 1 h. Then, NaBH_4 aqueous solution was quickly added under vigorous stirring for 2 h. Afterwards, the obtained suspension was centrifuged, washed thoroughly and dried in a vacuum oven at 60 °C for 12 h.

2.2. Characterization

X-ray diffraction (XRD) data of samples were obtained at room time on a Shimadzu XRD-6000 diffractometer, using Cu K α radiation ($k = 0.154 \text{ nm}$) at 30 mA, 40 kV, a scanning rate of 10° min^{-1} , and a 2 θ angle ranging from 3° to 70°.

Elemental analysis of metal in samples was performed using a Shimadzu ICP-7500 inductively coupled plasma emission spectrometer (ICP-AES) after the samples were dissolved in nitrohydrochloric acid.

Low-temperature N_2 adsorption-desorption isotherms of the samples were obtained on a Micromeritics ASAP 2020 sorptometer apparatus. The total specific surface areas were evaluated with the multi-point Brunauer-Emmett-Teller (BET) method.



Scheme 1. The synthetic procedure for RuCo/CoO_x catalyst.

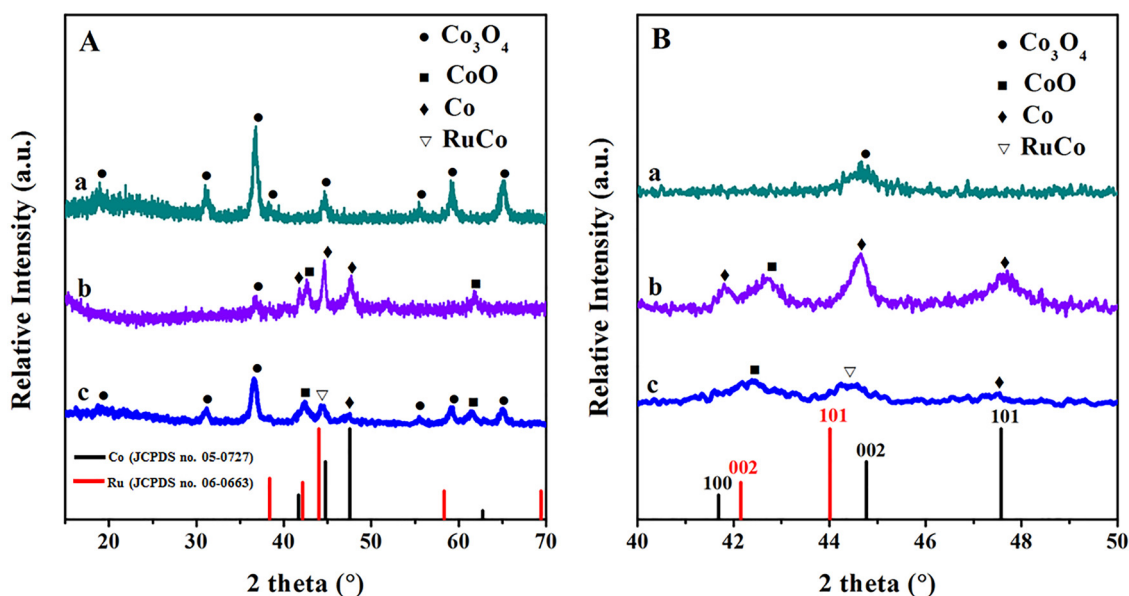


Fig. 1. XRD patterns (A) of Ru/Co₃O₄-B (a), Ru/Co/CoO_x-B (b) and RuCo/CoO_x (c), and detailed XRD patterns (B) of Ru/Co₃O₄-B (a), Ru/Co/CoO_x-B (b) and RuCo/CoO_x (c) in the 2θ range of 40°–50°.

The morphology of the samples was determined using a field emission scanning electron microscope (FE-SEM, Zeiss Supra 55 with an accelerating voltage of 20 kV) which was combined with energy-dispersive X-ray spectroscopy (EDX) performed using an Oxford Instruments INCA analyzer for determination of the metal composition.

Transmission electron microscopy (TEM) and high-resolution TEM (HRTEM) observations were carried out on a JEOL JEM-2100 transmission electron microscope with an accelerating voltage of 200 kV. A droplet of the ultrasonically dispersed powders was placed onto an amorphous carbon-coated copper grid and then dried at ambient temperature.

High-angle annular dark-field scanning TEM-energy-dispersive X-ray spectroscopy (HAADF-STEM-EDX) images were recorded on a JEOL2010F instrument.

X-ray photoelectron spectroscopy (XPS) measurements were performed using an ESCALAB 250 instrument (Thermo Electron) at a base pressure of 2×10^{-9} Pa with Al Kα radiation. The binding energy calibration of all spectra was referenced to the C1s signal at 284.6 eV.

The steady state photoluminescence (PL) spectra were obtained on RF-5301PC fluorescence spectrometer in the range of 220–500 nm with the excitation wavelength of 275 nm and the PMT voltage of 400 V. Both the excitation and emission slits are set to 3.0 nm.

H₂ temperature-programmed reduction (H₂-TPR) and H₂ temperature-programmed desorption (H₂-TPD) of the samples were performed using Micromeritics Chemisorb 2920 with a thermal conductivity detector (TCD). For H₂-TPR test, before measurement, the sample (100 mg) placed in a quartz U-tube reactor was degassed under flowing argon (50 mL/min) at 200 °C for 1 h and then cooled down to 50 °C. Finally, the TPR measure was performed in a stream of 10% v/v H₂/Ar (40 mL/min) with a heating rate of 10 °C min⁻¹ from 50 °C to 800 °C. In the case of H₂-TPD process, the reduced sample (100 mg) was firstly pretreated using the same procedure mentioned in H₂-TPR. After the sample cooled down to 50 °C, 10% v/v H₂/Ar flow (40 mL/min) was introduced to absorb sample for 1 h. Finally, Chemisorbed H₂ was desorbed by heating from 50 °C up to 600 °C at a temperature ramp of 10 °C/min.

TOF_{HMF} is defined as the moles of HMF converted per mole of Ru site per time, which was calculated according to the Eq. (1). TOF_{C-O}, as defined as the moles of C–O hydrogenolysis per mole of Ru site per time, was calculated based on the Eq. (2). The moles of C–O hydrogenolysis are defined as two-fold moles of DMF and DMTHF (total C–O

hydrogenolysis) plus moles of MFA (partial C–O hydrogenolysis). TOF_{DMF} is defined as the moles of generated DMF per mole of Ru site per time, which was calculated according to the Eq. (3). To obtain the intrinsic activity of catalysts, the HMF conversion was kept below 30%.

$$\text{TOF}_{\text{HMF}} = \frac{\text{Numbers of converted HMF (mol)}}{\text{Numbers of Ru sites (mol)} \cdot t \text{ (h)}} \quad (1)$$

$$\text{TOF}_{\text{C-O}} = \frac{\text{Numbers of C-O hydrogenolysis (mol)}}{\text{Numbers of Ru sites (mol)} \cdot t \text{ (h)}} \quad (2)$$

$$\text{TOF}_{\text{DMF}} = \frac{\text{Numbers of generated DMF (mol)}}{\text{Numbers of Ru sites (mol)} \cdot t \text{ (h)}} \quad (3)$$

2.3. Catalytic hydrogenolysis test

The hydrogenolysis of HMF was carried out using a 100 mL stainless steel autoclave equipped with a magnetic stirrer. In a typical experiment, 4 mmol HMF, 10 mL 1,4-dioxane and a certain amount of the catalyst were transferred into the reaction vessel. After closing the reactor, the air in the reaction reactor was purged out using H₂ at least ten times. Then the reactor was filled with H₂ to the required H₂ pressure. Subsequently, the reactor was initiated at the designed temperature under stirring. Upon completion of reaction for the set time, the reactor was cooled to room temperature and the pressure was released carefully. Finally, the liquid products were analyzed by an Agilent GC7890B gas chromatograph equipped with flame ionization detector and DB-WAX capillary column (30.0 m × 250 μm × 0.25 μm) and identified as compared with known standards using tridecane as an internal standard. In all cases, the carbon balances were above 96%. The injector temperature was set at 250 °C, and the detector column temperature was increased from 100 to 150 °C with a ramp rate of 5 °C min⁻¹.

3. Results and discussion

3.1. Structural analysis

As shown in Fig. S1, both Co₃O₄ support and RuO₂/Co₃O₄ catalyst precursor present a series of diffraction peaks at 31.3°, 36.8°, 38.5°, 44.8°, 55.7°, 59.4° and 65.2°, which belong to a characteristic feature of Co₃O₄ phase (JCPDS no. 43-1003). The diffraction intensity of RuO₂/

Table 1
The structural, textural and component properties of supported Ru samples.

Samples	Ru ^a (wt %)	Co ^a (wt %)	Co (0) ^b (at %)	Co(II) ^b (at %)	Co(III) ^b (at %)	Co(II)/(Co(III) + Co(II)) ratio ^b	Co(0)/Ru Ratio ^b	O _{II} /O _I ratio ^c	S _{BET} ^d (m ² g ⁻¹)
RuCo/CoO _x	1.6	63.7	14.0	40.0	46.0	0.47	9.5	1.6	96
Ru/Co ₃ O ₄ -B	1.7	56.3	0	35.0	65.0	0.35	0	0.9	48
Ru/Co/CoO _x -B	1.7	68.4	31.7	30.8	37.5	0.45	21.8	1.7	85

^a Determined by ICP-AES.

^b The proportions of different species on the surface measured by XPS.

^c Determined by XPS of O1s region.

^d BET surface area.

Co₃O₄ is weaker than that of Co₂O₃, implying that the introduction of Ru can decrease the crystal size of Co₃O₄. For reduced catalysts (Fig. 1A), Ru/Co₃O₄-B sample only exhibits the characteristic diffractions related to Co₃O₄ phase. No diffractions corresponding to metallic Ru phase can be observed in Ru-containing samples, suggestive of the highly dispersive nature of Ru species. Moreover, distinct XRD diffractions related to CoO, Co₃O₄ and metallic Co phases are detected in Ru/Co/CoO_x-B and RuCo/CoO_x samples, reflecting the reduction of Co₃O₄ and thus the formation of CoO_x support. Noticeably, only RuCo/CoO_x exhibits one peak between the (101) plane of metallic Ru phase and the (101) plane of metallic Co phase, indicating that the Co atom should be incorporated into the *fcc* structure of Ru⁰ to form an alloy phase with a concomitant lattice contraction [39–43], as further demonstrated by the detailed XRD patterns in the 2θ range of 40–50° (Fig. 1B). In addition, N₂ adsorption-desorption measurements and ICP-AES analysis reveal that RuCo/CoO_x sample possesses a higher specific surface area (96 m² g⁻¹) than other two supported Ru sample, despite a similar Ru loading (Table 1).

To gain insights into the metal-support interactions in different supported Ru samples, XPS characterization was performed. Since the C 1s region may partially overlap the Ru 3d_{3/2} region, the broad peak at 284.6 eV was fitted by two contributions at about 284.6 and 284.0 eV, which are assigned to C 1s and Ru 3d_{3/2} core levels, respectively. For RuCo/CoO_x, the Ru 3d_{5/2} signal appears at about 279.9 eV (Fig. 2A), which is typical of metallic Ru species [44]. The lower binding energy value for Ru 3d_{5/2} region in RuCo/CoO_x compared to those in Ru/Co₃O₄ and Ru/Co/CoO_x-B illustrates the electron-rich state of Ru⁰ species, due to the formation of strong metal-support electronic interaction and thus the electron transfer from CoO_x to Ru⁰ species. As shown in Fig. 2B, the XPS of Co 2p region presents two asymmetric main peaks at 775–790 and 790–810 eV, which correspond to Co 2p_{3/2} region and Co 2p_{1/2} region. The deconvolution for samples by Gaussian peak fitting reveals the existence of Co⁰, Co³⁺ and Co²⁺ species [45,46]. Table 1 summaries surface proportions of different Co species.

It is worthwhile to note that the Co²⁺/(Co²⁺ + Co³⁺) ratio in RuCo/CoO_x (0.47) or Ru/Co/CoO_x-B (0.45) is higher than that in the Ru/Co₃O₄-B (0.35), indicative of the reduction of Co³⁺ species. Meanwhile, surface Co⁰/Ru molar ratio in RuCo/CoO_x and Ru/Co₃O₄-B is as high as 9.5 and 21.8, respectively. Based on XRD and XPS results, it can be concluded that besides isolated metallic Co⁰ species, Co⁰ can alloy with Ru only in the RuCo/CoO_x sample, despite a higher Co⁰/Ru molar ratio in the Ru/Co/CoO_x-B. As shown in Fig. 2C, XPS spectra of O 1s region can be deconvoluted into two different surface oxygen species, O_I (530.6 eV) and O_{II} (532.4 eV), which are mainly related to the lattice oxygen species in the spinel structure and defect oxides (*i.e.* oxygen vacancies) or hydroxyl species [30], respectively. As listed in Table 1, the higher O_{II}/O_I intensity ratio for RuCo/CoO_x (1.6) and Ru/Co/CoO_x-B (1.7) than that for Ru/Co₃O₄-B (0.9) indicates the formation of more oxygen vacancies (O_v) on RuCo/CoO_x and Ru/Co/CoO_x-B samples through the following process of Co³⁺-O-Co³⁺ + H₂ → Co²⁺-O_v-Co²⁺ + H₂O during the reduction of Co₃O₄ support.

PL measurement was conducted over supported Ru samples under an excitation wavelength of 275 nm to further confirm the formation of oxygen vacancies. As shown in Fig. S2, an emission peak at approximately 368 nm should arise from the recombination of excitons on the surface defects, such as oxygen vacancies [47]. Additionally, it is seen that the PL intensities of RuCo/CoO_x and Ru/Co/CoO_x-B are equal but much stronger than that of Ru/Co₃O₄-B sample, mirroring a much higher concentration of surface oxygen vacancies, well in accordance with the above XPS results.

The morphology of the representative RuCo/CoO_x sample was investigated by SEM characterization. As shown in Fig. 3, RuCo/CoO_x presents a uniform dandelion-like morphology with a spiculate surface and a diameter of about 2.5 μm, which is similar to that of Ru/Co₃O₄-B (Fig. S3). Noticeably, the flower-like microsphere is constructed by a large quantity of closely packed thorn-like petals, thereby forming a highly porous micro/nanostructure. Such superstructure should favor the close contact of reactants with surface active sites during

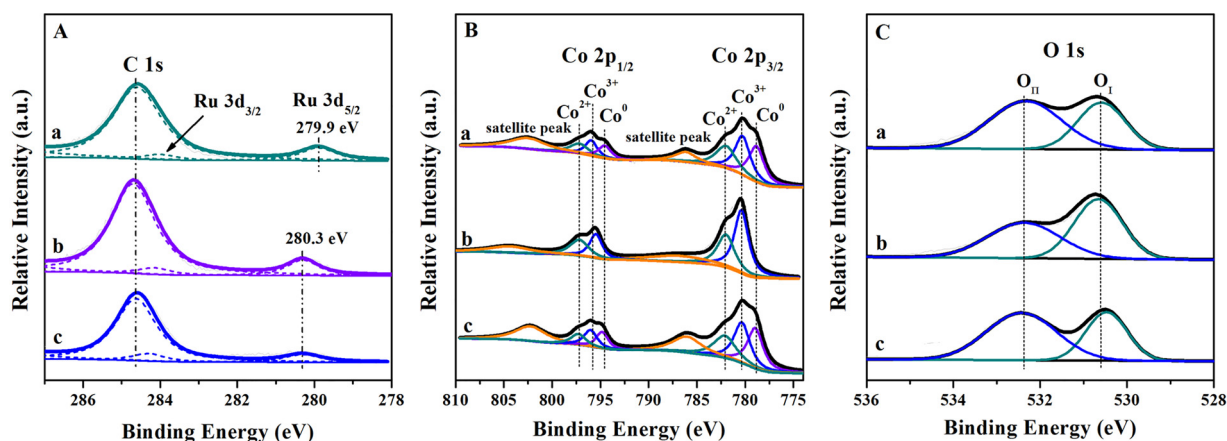


Fig. 2. XPS of Ru 3d (A), Co 2p (B) and O 1s (C) regions in RuCo/CoO_x (a), Ru/Co₃O₄-B (b) and Ru/Co/CoO_x-B (c) samples.

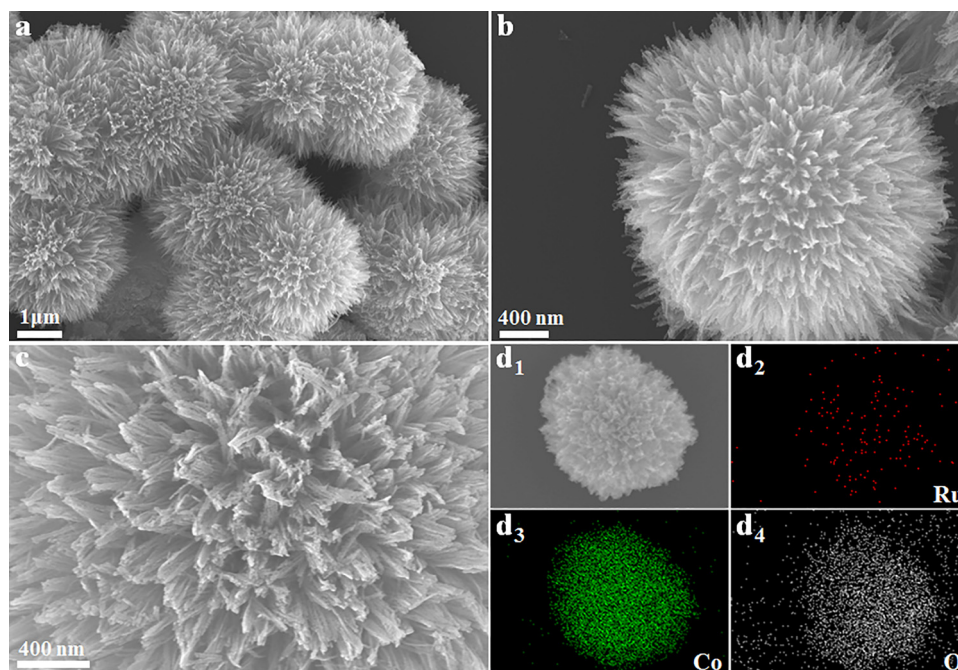


Fig. 3. SEM (a–c) of RuCo/CoO_x sample and elemental mapping (d) of Ru, Co and O elements.

heterogeneous reactions. Elemental mapping of RuCo/CoO_x catalyst depicts the homogeneous distributions of Ru, Co and O elements, demonstrating highly dispersive character of bimetallic RuCo NPs on the surface of dandelion-like CoO_x support.

Further, TEM observation reveals the well-defined dandelion-like micro/nanostructure of RuCo/CoO_x sample (Fig. 4a and b), where the highly dispersed back Ru or RuCo NPs is observed in Ru/Co₃O₄-B, Ru/Co/CoO_x-B or RuCo/CoO_x (Fig. S4). The average size of RuCo NPs in RuCo/CoO_x is 2.48 nm, which is slightly larger than those of Ru NPs in Ru/Co₃O₄-B (2.27 nm) and Ru/Co/CoO_x-B (2.25 nm). A HRTEM image of single petal on the RuCo/CoO_x clearly depicts the lattice fringes with 0.203 nm (Fig. 4c), which is slightly smaller than the (101) lattice spacing of metallic Ru phase but larger than the (101) lattice spacing of metallic Co phase. This result strongly confirms the formation of RuCo alloy phase [48]. Another clear lattice fringe with the interplanar spacings of about 0.246 nm is assignable to (111) plane of CoO phase. Moreover, the uniform distributions of Ru, Co and O elements are found according to the EDS mapping from HAADF-STEM image (Fig. 4d), while the STEM-EDX line scan spectra show the relative distributions of Ru, Co and O elements (Fig. 4e and f). It is clearly noted that Ru, Co and O lines show a similar distribution, despite a weaker signal of Ru element, illustrating the character of their close contact.

Reducibility of different samples was determined by H₂-TPR (Fig. 5). As reported in the literature, RuO₂ usually is reduced at about 100–230 °C [48–50]. For RuO₂/Co₃O₄ catalyst precursor, only a reduction peak at 366 °C is detected, owing to the overlapping of the reduction of Ru species with that of cationic Co species. This phenomenon reflects the presence of the strong Ru-Co interaction, which can result in the higher reduction temperature of cationic Ru species in RuO₂/Co₃O₄. Meanwhile, it is noted that the reduction temperature of Ru species in RuO₂/Co₃O₄ is also much higher than that in RuO₂/Al₂O₃, further demonstrating the stronger interactions between Ru species and the Co₃O₄ support. Such interactions can cause the simultaneous reduction of Ru and Co species and thus the formation of bimetallic RuCo NPs [51]. Notably, the reduction peak of RuO₂/Co₃O₄ shifts to the lower temperature in comparison with pure Co₃O₄ sample, which is an evidence of the obvious hydrogen spillover from easily reduced Ru^o species to Co₃O₄ support, implying the close contact and more interfacial sites between Ru and Co species because of the utilization of on-

pot embedding method [52]. As expected, the reduction temperature of Co₃O₄ is the same as that of Ru/Co₃O₄-B, demonstrating that the Ru^o species in Ru/Co₃O₄-B prepared using NaBH₄ reducing agent cannot induce the hydrogen spillover to Co₃O₄ support due to the relatively weak interaction between Ru^o species and Co₃O₄ support. A similar phenomenon on the Ru/Mn/Al₂O₃ system also was reported in the literature [53]. Moreover, the previous EXAFS study demonstrated that Ru existing in Co-Ru NPs could enhance the Co reducibility and promote the formation of Co-Ru alloy at low reduction temperature [54].

It is well known that for supported metal catalysts, the ability for the dissociation of H₂ and the hydrogen spillover have significant influences on the catalytic hydrogenation reactions [55], which can be determined by H₂-TPD characterization. As shown in Fig. 6, there are two broad peaks centered at approximately 132 and 275 °C in the H₂-TPD curve of RuCo/CoO_x sample. The low temperature peak is associated with H₂ chemisorption on RuCo NPs, while the high temperature peak is caused by the simultaneous desorption of H₂ chemisorption on Co NPs and spillover hydrogen absorbed on support surface [56,57]. H₂-TPD result of Co/CoO_x sample further proves that the desorption temperature of H₂ absorbed on Co NPs is relatively high (345 °C), probably due to the strong Co-H bonding. Notably, the amount of desorbed hydrogen over the RuCo/CoO_x at the high temperature is much larger than that over the Co/CoO_x, indicating a convincing evidence of hydrogen spillover from RuCo NPs to the CoO_x support. For Ru/Co/CoO_x-B and Ru/Co₃O₄-B references, a broad peak centered at 94 °C is correlated with H₂ chemisorption on Ru^o species. Considering the d-band electronic structure of transition metals, it is believed that the metal-hydrogen bonding energy on bimetallic RuCo NPs should be located between that of Ru-H and that of Co-H. Therefore, it can be rationally explained that the desorption temperature for chemisorbed hydrogen on bimetallic RuCo NPs (132 °C) is higher than that on monometallic Ru NPs (94 °C). Meanwhile, Ru/Co/CoO_x-B shows a small and broad desorption at about 390 °C, which represents the simultaneous desorption of spillover hydrogen and hydrogen absorbed on Co NPs. However, in the case of Ru/Co₃O₄-B sample, no desorption peak related to spillover hydrogen can be found at high temperature. Obviously, compared with Ru/Co/CoO_x-B and Ru/Co₃O₄-B samples, RuCo/CoO_x sample presents a greatly enhanced hydrogen spillover, probably due to strong interactions between RuCo NPs and CoO_x support, being beneficial for the

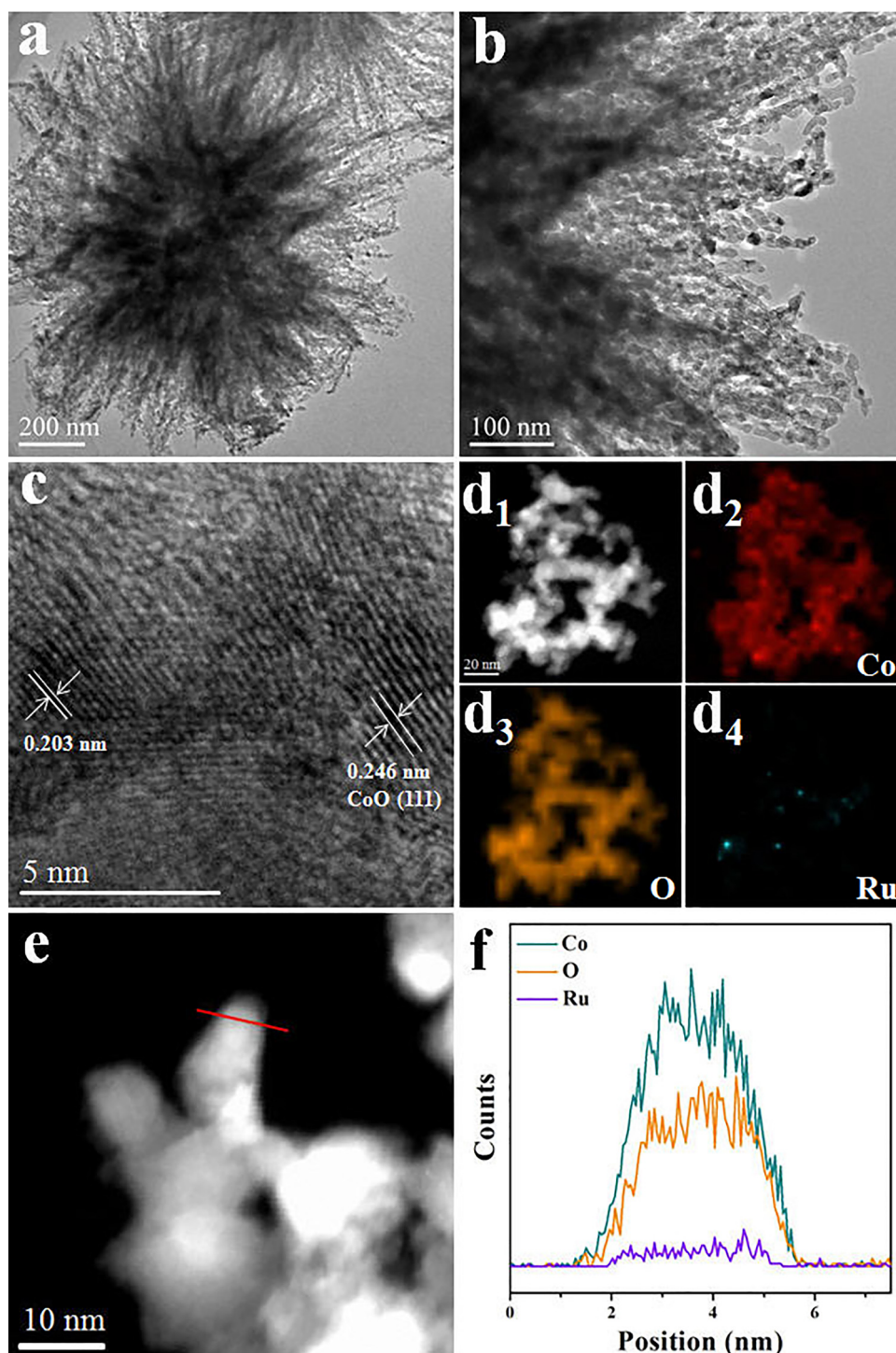


Fig. 4. HRTEM images (a–c) of RuCo/CoO_x sample. HAADF-STEM image (d) of RuCo/CoO_x with the EDX mapping of Co-K, O-K and Ru-K (d); EDX line scan spectra of Co-K, O-K and Ru-K along the red line in e (f) (For interpretation of the references to colour in this figure legend, the reader is referred to the web version of this article).

transfer of active hydrogen species on the RuCo/CoO_x. Additionally, more surface Co²⁺-O_v-Co²⁺ defects on the RuCo/CoO_x also may accelerate the reception of active hydrogen [55]. On the other hand, the amount of total desorbed H₂ over samples follows the order of RuCo/CoO_x > Ru/Co/CoO_x-B ≈ Ru/Co₃O₄-B > Co/CoO_x, indicating that RuCo/CoO_x possesses a strong ability for the dissociation of H₂, due to the presence of the electronic interaction between Ru-Co atoms in RuCo NPs.

3.2. Catalytic hydrogenolysis of HMF

Fig. 7 illustrates the effect of reaction time on the HMF hydrogenolysis of over different catalysts. It is seen that the HMF conversion and the DMF selectivity are gradually improved in the initial period of 2 h in all cases, accompanied by the transformation of intermediates BHMF and 5-methylfurfuryl alcohol (MFA) with the reaction time. Moreover, significant difference of catalytic performance in different catalysts is observed. After 2 h, RuCo/CoO_x catalyst yields a high DMF

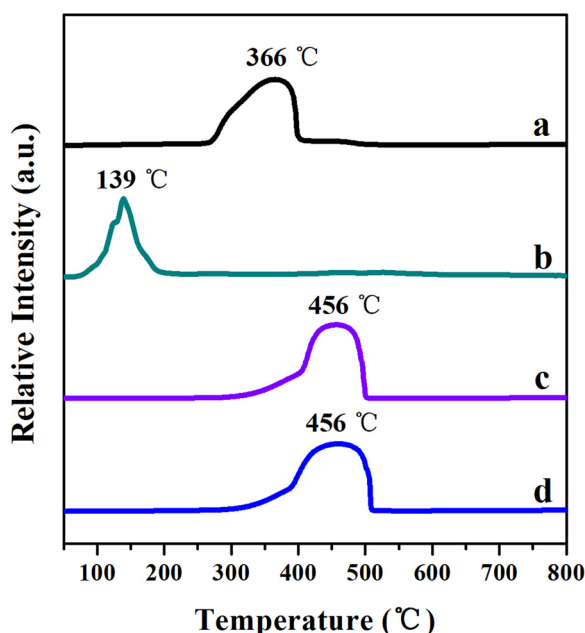


Fig. 5. H_2 -TPR profiles of $\text{RuO}_2/\text{Co}_3\text{O}_4$ (a), $\text{RuO}_2/\text{Al}_2\text{O}_3$ (b), Co_3O_4 (c) and $\text{Ru}/\text{Co}_3\text{O}_4\text{-B}$ (d) samples.

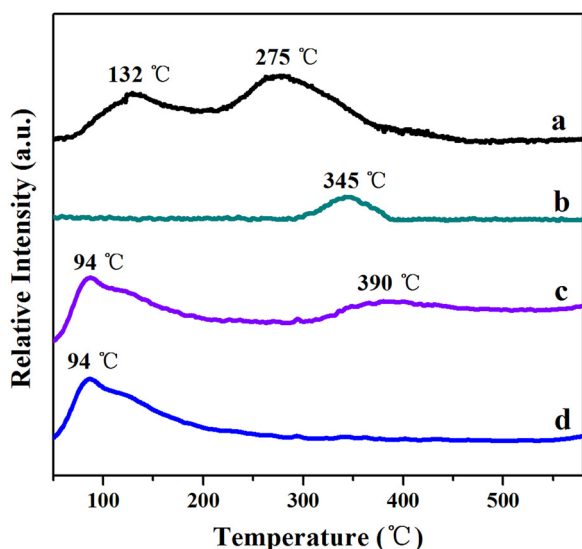


Fig. 6. H_2 -TPD profiles of RuCo/CoO_x (a), Co/CoO_x (b), $\text{Ru}/\text{Co}/\text{CoO}_x\text{-B}$ (c) and $\text{Ru}/\text{Co}_3\text{O}_4\text{-B}$ (d).

selectivity of 96.5% at a complete conversion of HMF. In contrast, $\text{Ru}/\text{Co}/\text{CoO}_x\text{-B}$ with abundant surface defects affords a relatively low HMF conversion of 90.4%, while a quite low conversion of 10.1% can be obtained over the Co/CoO_x . In addition, bimetallic RuCo/CoO_x catalyst also show higher HMF conversion compared with other two monometallic $\text{Ru}/\text{Co}_3\text{O}_4\text{-B}$ and $\text{Ru}/\text{Al}_2\text{O}_3$ catalysts. Above results demonstrate that bimetallic RuCo NPs formed on the RuCo/CoO_x catalyst can promote the HMF conversion. Notably, RuCo/CoO_x , $\text{Ru}/\text{Co}/\text{CoO}_x\text{-B}$ and Co/CoO_x all exhibit much higher DMF selectivity ($\sim 95\%$) than $\text{Ru}/\text{Co}_3\text{O}_4\text{-B}$ (75.3%) and $\text{Ru}/\text{Al}_2\text{O}_3$ (22.1%) after reaction of 2 h, suggesting that surface defects of catalysts can significantly benefit the hydrogenolysis of the hydroxyl group in HMF, BHMF and MFA.

The influence of reaction temperature and catalyst dosage on HMF hydrogenolysis over RuCo/CoO_x catalyst was explored. As shown in Fig. S5A, reaction temperature greatly impacts both the HMF conversion and DMF selectivity. RuCo/CoO_x catalyst only delivers HMF

conversion of 41.7% and DMF selectivity of 31.2% at 140 °C after reaction of 2 h. When the reaction temperature is elevated to 200 °C, HMF conversion and DMF selectivity can reach as high as 100% and 96.5%, respectively. Simultaneously, the main byproducts (BHMF and MFA) are rapidly transformed to DMF with the increase of reaction temperature, proving that high temperature can favor the hydrogenolysis of hydroxyl groups in HMF, BHMF and MFA. Catalyst dosage also exhibits a remarkable influence on HMF conversion and DMF selectivity (Fig. S5B). Relatively low HMF conversion (51.7%) and DMF selectivity (58.5%) are obtained for the catalyst of 0.04 g. Upon increasing the catalyst dosage from 0.04 g to 0.1 g, HMF conversion and DMF selectivity sharply improve to 100% and 96.5%, respectively. However, there is no continued increase in HMF conversion and DMF selectivity with further increase of the catalyst dosage to 0.12 g. These results demonstrate that the active catalytic sites of 0.1 g catalyst are sufficient for HMF hydrogenolysis.

In addition, the hydrogenolysis ability of RuCo/CoO_x catalyst was further explored using BHMF and furfural (FA) as substrates (Fig. S6). It is observed that with the prolonged reaction time up to 2 h, the conversion of BHMF or FA and selectivity of DMF or 2-methylfuran (MF) also are gradually improved. The yields of DMF and MF products can reach up to 98.5% and 98.3%, respectively, at 200 °C for 2 h, confirming the strong ability of RuCo/CoO_x for the hydrogenolysis of hydroxyl group.

Further, to get insights into the intrinsic activity of catalysts in HMF hydrogenolysis, the turnover frequency (TOF) of HMF conversion (TOF_{HMF}) or hydrogenolysis of C–O bonds ($\text{TOF}_{\text{C-O}}$) was calculated based on total Ru content determined by ICP-AES characterization at a low conversion level ($< 30\%$). As shown in Fig. 7E, the attained TOF_{HMF} value for RuCo/CoO_x reach as high as 420 h^{-1} , which is much higher than those for $\text{Ru}/\text{Co}/\text{CoO}_x\text{-B}$ (304 h^{-1}) and $\text{Ru}/\text{Co}_3\text{O}_4\text{-B}$ (290 h^{-1}). Noticeably, the $\text{TOF}_{\text{C-O}}$ value of RuCo/CoO_x (437 h^{-1}) is about 1.7 and 2.8 times higher than those of $\text{Ru}/\text{Co}/\text{CoO}_x\text{-B}$ (261 h^{-1}) and $\text{Ru}/\text{Co}_3\text{O}_4\text{-B}$ (155 h^{-1}), respectively. Moreover, RuCo/CoO_x shows a higher $\text{TOF}_{\text{C-O}}/\text{TOF}_{\text{HMF}}$ value (1.04) in compared with $\text{Ru}/\text{Co}/\text{CoO}_x\text{-B}$ (0.86) and $\text{Ru}/\text{Co}_3\text{O}_4\text{-B}$ (0.53). Considering a slight variation in the metal dispersion among these samples, as demonstrated by TEM observation (Fig. S4), the difference in catalytic performance of these catalysts may be not correlated with the metal dispersion in the present catalytic system. In addition, TOF_{DMF} value over RuCo/CoO_x was calculated based on the content of total precious metals obtained by ICP-AES characterization in initial reaction stage. As shown in Table S1, the TOF_{HMF} , $\text{TOF}_{\text{C-O}}$ and TOF_{DMF} values over the RuCo/CoO_x can reach 420 h^{-1} , 437 h^{-1} and 220 h^{-1} , respectively, which are higher than or comparable to those over other precious metal-based catalysts reported in the literature.

As depicted in Fig. S7, $-\ln(1-x)$ (x = HMF conversion) increases linearly with the reaction time over different catalysts at 160 °C, 180 °C and 200 °C. Thus, the hydrogenolysis of HMF follows first-order kinetics in the present Ru-based catalyst system. The apparent activation energies (E_a) were determined for further understanding the intrinsic activity of RuCo/CoO_x , $\text{Ru}/\text{Co}/\text{CoO}_x\text{-B}$ and $\text{Ru}/\text{Co}_3\text{O}_4\text{-B}$ catalysts based on the calculated reaction rate constants (k) at different temperatures (Fig. S8A). RuCo/CoO_x presents the lowest apparent activation energy (55 kJ/mol) compared to $\text{Ru}/\text{Co}/\text{CoO}_x\text{-B}$ (61 kJ/mol) and $\text{Ru}/\text{Co}_3\text{O}_4\text{-B}$ (67 kJ/mol), indicating the unique ability of RuCo/CoO_x for HMF hydrogenolysis (Fig. S8B).

As reported by our group, surface defect (*i.e.*, oxygen vacancies, Co^{2+} species) of catalyst can promote the activation of C=O bond in reactant molecule [29,30]. To verify the activation form of C=O and C–O bonds of HMF molecule on different samples, furfural and furfuryl alcohol were served as model molecules to replace HMF for *in situ* FT-IR absorption characterization. As shown in Fig. 8A, $\text{Ru}/\text{Co}_3\text{O}_4\text{-B}$ sample only presents one absorption peak at 1718 cm^{-1} , which is related to the stretching vibration of the C=O bond in physisorbed furfural. The absorption band at low wavenumber (1670 cm^{-1}) detected in $\text{RuCo}/$

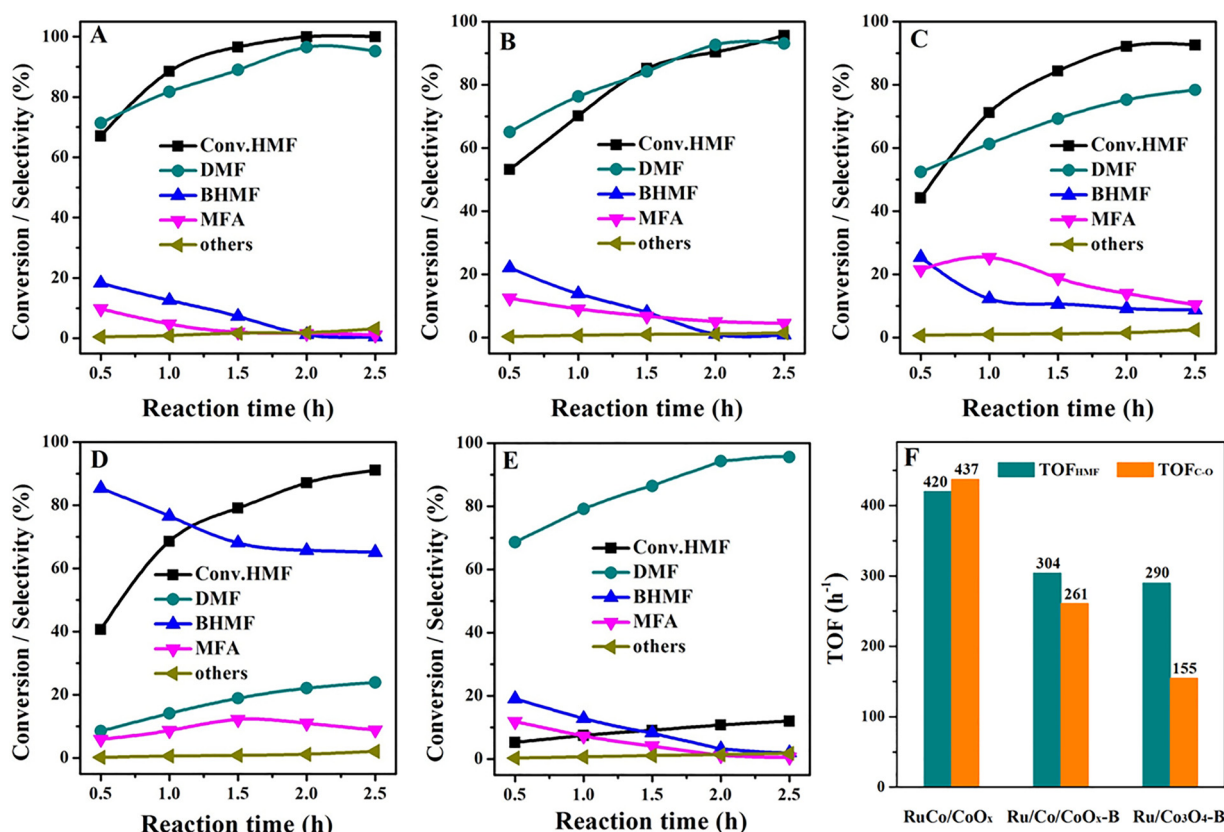


Fig. 7. The conversion and product selectivities with the reaction time on the HMF hydrogenolysis of over RuCo/CoO_x (A), Ru/Co/CoO_x-B (B), Ru/Co₃O₄-B (C), Ru/Al₂O₃ (D) and Co/CoO_x (E). TOF_{HMF} and TOF_{C-O} values over different samples (F). TOF_{HMF} was calculated based on converted HMF and TOF_{C-O} was calculated based on DMF and MFA products after reaction of 10 min. Reaction conditions: catalyst, 0.1 g; HMF, 4 mmol; 1,4-dioxane, 10 mL; reaction temperature, 200 °C; H₂ pressure, 0.5 Mpa. ^b Others mainly include 2,5-dimethyltetrahydrofuran, tetrahydrofuran and C-C cracking products.

CoO_x and Ru/Co/CoO_x-B samples indicates the decrease of C=O bond energy, attributable to the activation of C=O bond by large quantities of surface defects. *In situ* FT-IR spectra of furfuryl alcohol adsorption on different samples are presented in Fig. 8B. All samples exhibit one absorption peak at 1008 cm⁻¹, which belongs to the stretching vibration of the C–O–C bond in furan ring. As for Ru/Co₃O₄-B sample, the band

at 1076 cm⁻¹ is associated with C–O bond of CH₂–OH in physisorbed furfuryl alcohol. Noticeably, the stretching band of C–O bond red-shift by about 14 cm⁻¹ in RuCo/CoO_x and Ru/Co/CoO_x-B samples, implying the weakening of C–O bond. Above results demonstrate that surface defects can effectively activate C=O and C–O bonds, which can play a vital role in the hydrogenolysis of HMF to produce DMF.

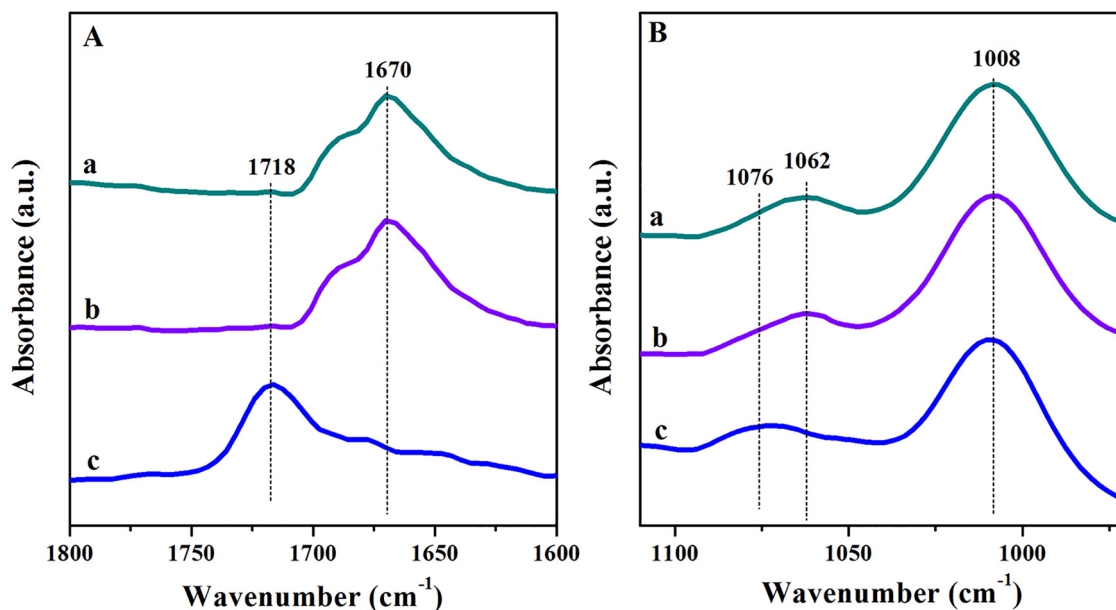
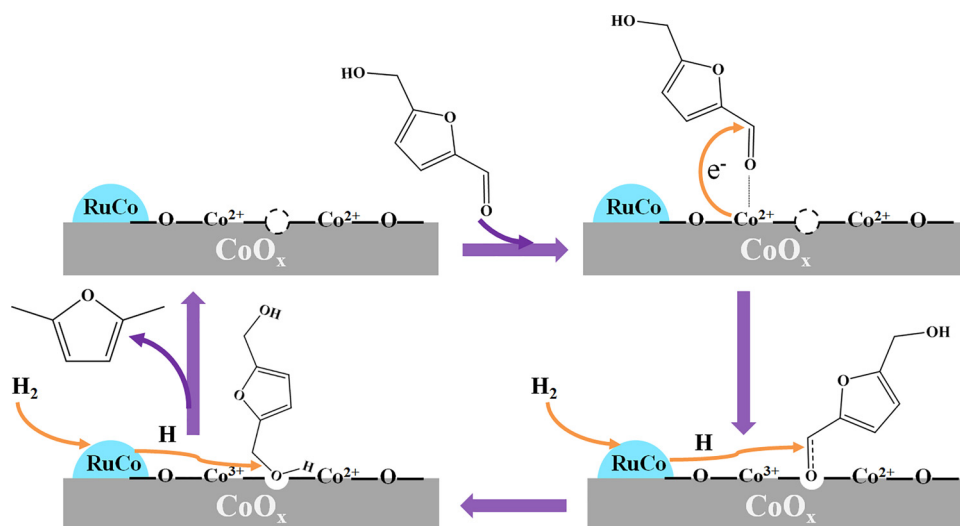


Fig. 8. *In-situ* FT-IR spectra of furfural (A) and furfuryl alcohol (B) absorption on RuCo/CoO_x (a), Ru/Co/CoO_x-B (b) and Ru/Co₃O₄-B (c) samples.



Scheme 2. Proposed possible reaction mechanism of HMF hydrogenolysis to produce DMF over the RuCo/CoO_x catalyst.

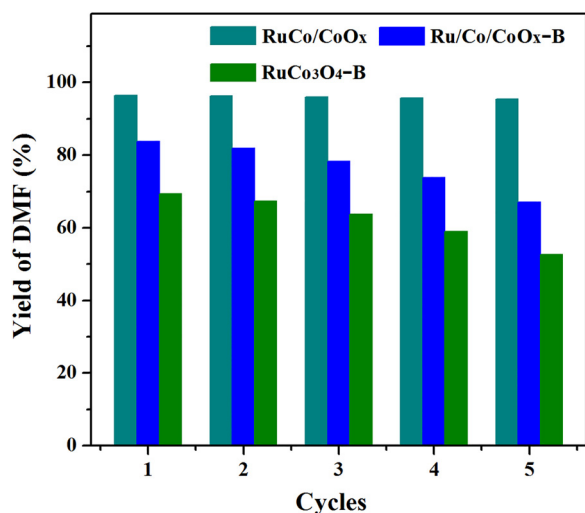


Fig. 9. The reusability of different catalysts in the hydrogenolysis of HMF. Reaction conditions: catalyst, 0.1 g; HMF, 4 mmol; 1,4-dioxane, 10 mL; reaction temperature, 200 °C; reaction time, 2 h; 0.5 MPa H₂.

Based on above mentioned characterizations and catalytic performance results, a plausible mechanism of HMF hydrogenolysis over the RuCo/CoO_x is proposed (Scheme 2). For the catalytic HMF hydrogenolysis over the RuCo/CoO_x, firstly, surface Co²⁺ species next to oxygen vacancies may fix the oxygen atom of carbonyl group in HMF through electron transfer, thereby leading to the formation of Co³⁺ species and thus a weakening of the carbonyl group. Subsequently, the oxygen atom of the weakened carbonyl group in HMF can occupy the oxygen vacancy adjacent to Co³⁺. Such interaction between HMF and surface Co²⁺–O_v–Co²⁺ defective structures can significantly promote the chemisorption of HMF, as evidenced by *in situ* FT-IR characterization, and thus being beneficial for the hydrogenation of C=O bond in HMF. Simultaneously, surface bimetallic RuCo NPs bearing strong Ru–Co interactions can more easily dissociate H₂ to generate active hydrogen species, compared with Ru or Co monometallic NPs in Ru/Co/CoO_x-B, Ru/Co₃O₄-B, Ru/Al₂O₃ or Co/CoO_x references. Further, the formed active hydrogen species may rapidly spill to the support surface due to the close contact of RuCo NPs and CoO_x support, as evidenced by above H₂-TPR and H₂-TPD results, thus promoting the hydrogenation of C=O bond to form alcohol hydroxyl group. Finally, the formed alcohol hydroxyl group can be further activated by oxygen vacancies and

converted to desired target product with the help of bimetallic RuCo NPs. In a way, as-formed RuCo/CoO_x with the distinct dandelion-like superstructure can provide more exposed adsorption and active sites, promoting the HMF hydrogenolysis. As a result, the enhanced catalytic performance of RuCo/CoO_x in the HMF hydrogenolysis to produce DMF should be attributable to the unique synergy between bimetallic RuCo NPs and surface Co²⁺–O_v–Co²⁺ defects at the metal-support interface, as well as the enhanced hydrogen spillover effect and the dandelion-like superstructure of the catalyst. Moreover, the Co NPs in RuCo/CoO_x are negligibly active for HMF conversion, as evidenced by the catalytic result of Co/CoO_x in Fig. 7E, demonstrating that the high HMF conversion in RuCo/CoO_x is ascribed to bimetallic RuCo NPs. From the *in situ* FT-IR spectra of furfural and furfuryl alcohol adsorption, it can be reasonably deduced that the surface defects benefit the activation of C=O and C–O bonds in HMF. Furthermore, abundant active hydrogen on the support surface that originates from the hydrogen spillover effect will rapidly converted activated HMF to desired DMF, thus improving the selectivity of DMF, which has been proved by the catalytic results of CoO_x-supported samples (RuCo/CoO_x, Ru/Co/CoO_x-B and Co/CoO_x) in Fig. 7. In a way, the electron-rich Ru species that derive from the strong metal-support interaction may promote the activation the C=O group in HMF [58].

The reusability of different samples was tested for the hydrogenolysis of HMF to produce DMF (Fig. 9). As expected, RuCo/CoO_x catalyst still can keep excellent catalytic performance after recycling five times. The yield of DMF only decreases by about 1.0%, which may be ascribed to the catalyst loss during post-processing. But, in the case of Ru/Co₃O₄-B and Ru/Co/CoO_x-B, the DMF yield decreases by as high as 24.1% and 20.0%, respectively. To further understand the deactivation mechanism, ICP-AES measurement was carried out to determine the Ru contents in fresh and the spent (five cycles) catalysts. The results show that the Ru leaching loss in RuCo/CoO_x is about 1.0 wt% of the total Ru content. In contrast, Ru leaching is considerably higher for Ru/Co₃O₄-B and Ru/Co/CoO_x-B catalysts, which can reach 11.8 wt% and 10.4 wt%. The results clearly indicate that the embedding method can significantly inhibit the leaching of Ru particles due to the strong interaction between RuCo bimetal NPs and CoO_x support.

4. Conclusions

In summary, a simple and effective embedding method was developed for the fabrication of RuCo bimetallic NPs inside dandelion-like CoO_x microspheres structure with large quantities of surface defects (i.e. Co²⁺ species and oxygen vacancies) simultaneously constructed.

As-formed RuCo/CoO_x bimetallic catalyst exhibited excellent catalytic performance for the hydrogenolysis of HMF to produce DMF (96.5% yield after 2 h) even when the HMF/Ru molar ratio was as high as 252.7, comparable to those of previously reported catalysts or even better. Particularly, RuCo/CoO_x also showed a high TOF_{HMF} (420 h⁻¹), TOF_{C=O} (437 h⁻¹) and TOF_{DMF} (220 h⁻¹), as well as low apparent activation energy (55 kJ/mol). Characteristic studies verified that the strong interaction between Ru species and support enabled RuCo bimetallic NPs and abundant surface defects (i.e., oxygen vacancies, Co²⁺ species) on CoO_x support, which could facilitate the dissociation of H₂ to active hydrogen and subsequent spillover to support, as well as absorption and activation of C=O bond in HMF, accounting for high HMF conversion and DMF selectivity. Furthermore, the catalyst exhibited enhanced stability in the hydrogenolysis of HMF and a high efficiency for hydrogenolysis of FA and BHMF. The attractive features of RuCo/CoO_x might be also promising for hydrogenolysis of lignin-derived model compounds, providing guiding principles for future catalyst design in the field of biomass upgrading.

Acknowledgments

We gratefully thank the financial support from National Natural Science Foundation of China (21776017; 21521005) and the Fundamental Research Funds for the Central Universities (buctrc201528).

Appendix A. Supplementary data

Supplementary material related to this article can be found, in the online version, at doi:<https://doi.org/10.1016/j.apcatb.2018.06.026>.

References

- J.N. Chheda, G.W. Huber, J.A. Dumesic, Liquid-phase catalytic processing of biomass-derived oxygenated hydrocarbons to fuels and chemicals, *Angew. Chem. Int. Ed.* 46 (2007) 7164–7183.
- J.B. Binder, R.T. Raines, Simple chemical transformation of lignocellulosic biomass into furans for fuels and chemicals, *J. Am. Chem. Soc.* 131 (2009) 1979–1985.
- Hu Li, Tingting Yang, Zhen Fang, Biomass-derived mesoporous Hf-containing hybrid for efficient Meerwein Ponndorf-Verley reduction at low temperatures, *Appl. Catal. B: Environ.* 227 (2018) 79–89.
- A. Corma, S. Iborra, A. Vely, Chemical routes for the transformation of biomass into chemicals, *Chem. Rev.* 107 (2007) 2411–2502.
- L.S. Ribeiro, J.J. Delgado, J.J.M. Órfão, M.F.R. Pereira, Carbon supported Ru-Ni bimetallic catalysts for the enhanced one-pot conversion of cellulose to sorbitol, *Appl. Catal. B: Environ.* 217 (2017) 265–274.
- K. Shimizu, A. Satsuma, Toward a rational control of solid acid catalysis for green synthesis and biomass conversion, *Energy Environ. Sci.* 4 (2011) 3140–3153.
- R. Karinen, K. Vilonen, M. Niemelä, Biorefining: heterogeneously catalyzed reactions of carbohydrates for the production of furfural and hydroxymethylfurfural, *ChemSusChem* 4 (2011) 1002–1016.
- J. Wu, G. Gao, J.L. Li, P. Sun, X.D. Long, F.W. Li, Efficient and versatile CuNi alloy nanocatalysts for the highly selective hydrogenation of furfural, *Appl. Catal. B: Environ.* 203 (2017) 227–236.
- H.L. Liu, Z.W. Huang, H.X. Kang, X.M. Li, C.G. Xia, J. Chen, H.C. Liu, Efficient bimetallic NiCu-SiO₂ catalysts for selective hydrogenolysis of xylitol to ethylene glycol and propylene glycol, *Appl. Catal. B: Environ.* 220 (2018) 251–263.
- Y. Román-Leshkov, J.N. Chheda, J.A. Dumesic, Phase modifiers promote efficient production of hydroxymethylfurfural from fructose, *Science* 312 (2006) 1933–1937.
- X. Kong, Y.F. Zhu, H.Y. Zheng, X.Q. Li, Y.L. Zhu, Y.-W. Li, Ni nanoparticles inlaid nickel phyllosilicate as a metal-acid bifunctional catalyst for low-temperature hydrogenolysis reactions, *ACS Catal.* 5 (2015) 5914–5920.
- B. Chen, F. Li, Z. Huang, G. Yuan, Carbon-coated Cu-Co bimetallic nanoparticles as selective and recyclable catalysts for production of biofuel 2,5-dimethylfuran, *Appl. Catal. B: Environ.* 200 (2017) 192–199.
- L.C. Gao, K.J. Deng, J.D. Zheng, B. Liu, Z.H. Zhang, Efficient oxidation of biomass derived 5-hydroxymethylfurfural into 2,5-furandicarboxylic acid catalyzed by Merrifield resin supported cobalt porphyrin, *Chem. Eng. J.* 270 (2015) 444–449.
- D.X. Yan, J.Y. Xin, C.Y. Shi, X.M. Lu, L.L. Ni, G.Y. Wang, S.J. Zhang, Base-free conversion of 5-hydroxymethylfurfural to 2,5-furandicarboxylic acid in ionic liquids, *Chem. Eng. J.* 323 (2017) 473–482.
- Y. Román-Leshkov, C.J. Barrett, Z.Y. Liu, J.A. Dumesic, Production of dimethylfuran for liquid fuels from biomass-derived carbohydrates, *Nature* 447 (2007) 982–985.
- X.X. Liu, J.F. Xiao, H. Ding, W.Z. Zhong, Q. Xu, S.P. Su, D. Yin, Catalytic aerobic oxidation of 5-hydroxymethylfurfural over VO²⁺ and Cu²⁺ immobilized on amino functionalized SBA-15, *Chem. Eng. J.* 283 (2016) 1315–1321.
- X. Kong, R.X. Zheng, Y.F. Zhu, G.Q. Ding, Y.L. Zhu, Y.W. Wang, Rational design of Ni-based catalysts derived from hydrotalcite for selective hydrogenation of 5-hydroxymethylfurfural, *Green Chem.* 17 (2015) 2504–2514.
- Z. Gao, C.Y. Li, G.L. Fan, L. Yang, F. Li, Nitrogen-doped carbon-decorated copper catalyst for highly efficient transfer hydrogenolysis of 5-hydroxymethylfurfural to convertibly produce 2,5-dimethylfuran or 2,5-dimethyltetrahydrofuran, *Appl. Catal. B: Environ.* 226 (2018) 523–533.
- C.M. Zhou, W.P. Deng, X.Y. Wan, Q.H. Zhang, Y.H. Yang, Y. Wang, Functionalized carbon nanotubes for biomass conversion: the base-free aerobic oxidation of 5-hydroxymethylfurfural to 2,5-furandicarboxylic acid over platinum supported on a carbon nanotube catalyst, *ChemCatChem* 7 (2015) 2853–2863.
- A.S. Nagpure, A.K. Venugopal, N. Lucas, M. Manikandan, R. Thirumalaiswamy, S. Chilukuri, Renewable fuels from biomass-derived compounds: Ru-containing hydrotalcites as catalysts for conversion of HMF to 2,5-dimethylfuran, *Catal. Sci. Technol.* 5 (2015) 1463–1472.
- T. Thananathanachon, T.B. Rauchfuss, Efficient production of the liquid fuel 2,5-dimethylfuran from fructose using formic acid as a reagent, *Angew. Chem.* 122 (2010) 6766–6768.
- G.-H. Wang, J. Hilgert, F.H. Richter, F. Wang, H.-J. Bongard, B. Splietho, C. Weidenthaler, F. Schüth, Platinum-cobalt bimetallic nanoparticles in hollow carbon nanospheres for hydrogenolysis of 5-hydroxymethylfurfural, *Nat. Mater.* 13 (2014) 293–300.
- M. Chidambaram, A.T. Bell, A two-step approach for the catalytic conversion of glucose to 2,5-dimethylfuran in ionic liquids, *Green Chem.* 12 (2010) 1253–1262.
- B. Saha, C.M. Bohn, M.M. Abu-Omar, Zinc-assisted hydrodeoxygenation of biomass-derived 5-hydroxymethylfurfural to 2,5-dimethylfuran, *ChemSusChem* 7 (2014) 3095–3101.
- L. Hu, X. Tang, J.X. Xu, Z. Wu, L. Lin, S.J. Liu, Selective transformation of 5-hydroxymethylfurfural into the liquid fuel 2,5-dimethylfuran over carbon-supported ruthenium, *Ind. Eng. Chem. Res.* 53 (2014) 3056–3064.
- T.S. Hansen, K. Barta, P. Anastas, P.C. Ford, A. Riisager, One-pot reduction of 5-hydroxymethylfurfural via hydrogen transfer from supercritical methanol, *Green Chem.* 14 (2012) 2457–2461.
- J. Anton, J. Nebel, H.Q. Song, C. Froese, P. Weide, H. Ruland, M. Muhler, S. Kaluza, The effect of sodium on the structure-activity relationships of cobalt-modified Cu/ZnO/Al₂O₃ catalysts applied in the hydrogenation of carbon monoxide to higher alcohols, *J. Catal.* 335 (2016) 175–186.
- D. Albani, M. Capdevila-Cortada, G. Vile, S. Mitchell, O. Martin, N. Lopez, J. Perez-Ramirez, Semihydrogenation of acetylene on indium oxide: proposed single-ensemble catalysis, *Angew. Chem.* 129 (2017) 10895–10900.
- Z. Gao, L. Yang, G.L. Fan, F. Li, Promotional role of surface defects on carbon-supported ruthenium-based catalysts in the transfer hydrogenation of furfural, *ChemCatChem* 8 (2016) 3769–3779.
- Q. Hu, L. Yang, G.L. Fan, F. Li, Hydrogenation of biomass-derived compounds containing a carbonyl group over a copper-based nanocatalyst: insight into the origin and influence of surface oxygen vacancies, *J. Catal.* 340 (2016) 184–195.
- K.A. Resende, C.A. Teles, G. Jacobs, B.H. Davis, D.C. Cronauer, A.J. Kropf, C.L. Marshall, C.E. Hori, F.B. Noronha, Hydrodeoxygenation of phenol over zirconia supported Pd bimetallic catalysts. The effect of second metal on catalyst performance, *Appl. Catal. B: Environ.* 232 (2018) 213–231.
- F. Tao, S. Zhang, L. Nguyen, X.Q. Zhang, Action of bimetallic nanocatalysts under reaction conditions and during catalysis: evolution of chemistry from high vacuum conditions to reaction conditions, *Chem. Soc. Rev.* 41 (2012) 7980–7993.
- A. Borgna, B.G. Anderson, A.M. Saib, H. Bluhm, M. Havecker, A. Knop-Gericke, A.E.T. Kuiper, Y. Tammimga, J.W. Niemantsverdriet, Pt-Co/SiO₂ bimetallic planar model catalysts for selective hydrogenation of crotonaldehyde, *J. Phys. Chem. B* 108 (2004) 17905–17914.
- S.C. Tsang, N. Cailuo, W. Odoro, A.T.S. Kong, L. Clifton, K.M.K. Yu, B. Thiebaud, J. Cookson, P. Bishop, Engineering preformed cobalt-doped platinum nanocatalysts for ultrasensitive hydrogenation, *ACS Nano* 2 (2008) 2547–2553.
- B.H. Wu, H.Q. Huang, J. Yang, N.F. Zheng, G. Fu, Selective hydrogenation of α,β -unsaturated aldehydes catalyzed by amine-capped platinum-cobalt nanocrystals, *Angew. Chem. Int. Ed.* 124 (2012) 3496–3499.
- Y. Mikami, A. Dhakshinamoorthy, M. Alvaro, H. García, Catalytic activity of unsupported gold nanoparticles, *Catal. Sci. Technol.* 3 (2013) 58–69.
- D. Astruc, F. Lu, J.R. Aranzas, Nanoparticles as recyclable catalysts: the frontier between homogeneous and heterogeneous catalysis, *Angew. Chem. Int. Ed.* 44 (2005) 7852–7872.
- S.F. Cai, H.H. Duan, H.P. Rong, D.S. Wang, L.S. Li, W. He, Y.D. Li, Highly active and selective catalysis of bimetallic Rh₃Ni₁ nanoparticles in the hydrogenation of nitroarenes, *ACS Catal.* 3 (2013) 608–612.
- J. Ying, J. Li, G.P. Jiang, Z.P. Cano, Z. Ma, C. Zhong, D. Su, Z.W. Chen, Metal-organic frameworks derived platinum-cobalt bimetallic nanoparticles in nitrogen-doped hollow porous carbon capsules as a highly active and durable catalyst for oxygen reduction reaction, *Appl. Catal. B: Environ.* 225 (2018) 496–503.
- S.I. Lim, M. Varon, I. Ojea-Jimenez, J. Arbiol, V. Puentes, Exploring the limitations of the use of competing reducers to control the morphology and composition of Pt and PtCo nanocrystals, *Chem. Mater.* 22 (2010) 4495–4504.
- S.H. Liu, F.S. Zheng, J.R. Wu, Preparation of ordered mesoporous carbons containing well-dispersed and highly alloying Pt-Co bimetallic nanoparticles toward methanol-resistant oxygen reduction reaction, *Appl. Catal. B: Environ.* 108 (2011) 81–89.
- J.F. Xu, X.Y. Liu, Y. Chen, Y.M. Zhou, T.H. Lu, Y.W. Tang, Platinum-cobalt alloy

- networks for methanol oxidation electrocatalysis, *J. Mater. Chem.* 22 (2012) 23659–23667.
- [43] D.L. Wang, H.L. Xin, R. Hovden, H.S. Wang, Y.C. Yu, D.A. Muller, F.J. DiSalvo, H.D. Abruña, Structurally ordered intermetallic platinum-cobalt core-shell nanoparticles with enhanced activity and stability as oxygen reduction electrocatalysts, *Nat. Mater.* 12 (2013) 81–87.
- [44] D. Albani, Q. Li, G. Vilé, S. Mitchell, N. Almora-Barrios, P.T. Witte, N. López, J. Pérez-Ramírez, Interfacial acidity in ligand-modified ruthenium nanoparticles boosts the hydrogenation of levulinic acid to gamma-valerolactone, *Green Chem.* 19 (2017) 2361–2370.
- [45] X.H. Liu, L.J. Xu, G.Y. Xu, W.D. Jia, Y.F. Ma, Y. Zhang, Selective hydrodeoxygenation of lignin-derived phenols to cyclohexanols or cyclohexanes over magnetic CoN_x/NC catalysts under mild conditions, *ACS Catal.* 6 (2016) 7611–7620.
- [46] J. Deng, H.J. Song, M.S. Cui, Y.P. Du, Y. Fu, Aerobic oxidation of hydroxymethylfurfural and furfural by using heterogeneous $\text{Co}_3\text{O}_4\text{-N@C}$ catalysts, *ChemSusChem* 7 (2014) 3334–3340.
- [47] V. Gurylev, C.Y. Su, T.P. Perng, Surface reconstruction, oxygen vacancy distribution and photocatalytic activity of hydrogenated titanium oxide thin film, *J. Catal.* 330 (2015) 177–186.
- [48] B.D. Li, J. Wang, Y.Z. Yuan, H. Ariga, S. Takakusagi, K. Asakura, Carbon nanotube-supported RuFe bimetallic nanoparticles as efficient and robust catalysts for aqueous-phase selective hydrogenolysis of glycerol to glycols, *ACS Catal.* 1 (2011) 1521–1528.
- [49] M. Ishikawa, M. Tamura, Y. Nakagawa, K. Tomishige, Demethoxylation of guaiacol and methoxybenzenes over carbon-supported Ru–Mn catalyst, *Appl. Catal. B: Environ.* 182 (2016) 193–203.
- [50] M. Balaraju, V. Rekha, B.L.A. Prabhavathi Devi, R.B.N. Prasad, P.S. Sai Prasad, N. Lingaiah, Surface and structural properties of titania-supported Ru catalysts for hydrogenolysis of glycerol, *Appl. Catal. A: Gen.* 384 (2010) 107–114.
- [51] Z.J. Mei, Y. Li, M.H. Fan, M.D. Argyle, J.K. Tang, The effects of bimetallic Co–Ru nanoparticles on $\text{Co}/\text{RuO}_2/\text{Al}_2\text{O}_3$ catalysts for the water gas shift and methanation, *Int. J. Hydrogen Energy* 39 (2014) 14808–14816.
- [52] J.S. Jung, J.S. Lee, G. Choi, S. Ramesha, D.J. Moona, The characterization of microstructure of cobalt on $\gamma\text{-Al}_2\text{O}_3$ for FTS: effects of pretreatment on Ru–Co/ $\gamma\text{-Al}_2\text{O}_3$, *Fuel* 149 (2015) 118–129.
- [53] M. Nurunnabi, K. Murata, K. Okabe, M. Inaba, I. Takahara, Performance and characterization of Ru/ Al_2O_3 and Ru/ SiO_2 catalysts modified with Mn for Fischer-Tropsch synthesis, *Appl. Catal. A: Gen.* 340 (2008) 203–211.
- [54] H. Kusaka, Y. Hara, M. Onuki, T. Akai, M. Okuda, Characterization and nitrile group hydrogenation study of supported and unsupported Ru–Co catalyst, *J. Catal.* 161 (1996) 96–106.
- [55] J.W. Zheng, X.P. Duan, H.Q. Lin, Z.Q. Gu, H.H. Fang, J.H. Li, Y.Z. Yuan, Silver nanoparticles confined in carbon nanotubes: on the understanding of the confinement effect and promotional catalysis for the selective hydrogenation of dimethyl oxalate, *Nanoscale* 8 (2016) 5959–5967.
- [56] A.M. Hilmen, D. Schanke, K.F. Hanssen, A. Holmen, Study of the effect of water on alumina supported cobalt Fischer-Tropsch catalysts, *Appl. Catal. A: Gen.* 186 (1999) 169–188.
- [57] J.T. Miller, B.L. Meyers, M.K. Barr, F.S. Modica, D.C. Koningsberger, Hydrogen temperature-programmed desorptions in platinum catalysts: decomposition and isotopic exchange by spillover hydrogen of chemisorbed ammonia, *J. Catal.* 159 (1996) 41–49.
- [58] J.J. Tan, J.L. Cui, X.J. Cui, T.S. Deng, X.Q. Li, Y.L. Zhu, Y.W. Li, Graphene-modified Ru nanocatalyst for low-temperature hydrogenation of carbonyl groups, *ACS Catal.* 5 (2015) 7379–7384.